

# Soil Diversity and Hydration as Observed by ChemCam at Gale Crater, Mars

P.-Y. Meslin,<sup>1,2\*</sup> O. Gasnault,<sup>1,2</sup> O. Forni,<sup>1,2</sup> S. Schröder,<sup>1,2</sup> A. Cousin,<sup>3</sup> G. Berger,<sup>1,2</sup> S. M. Clegg,<sup>3</sup> J. Lasue,<sup>1,2</sup> S. Maurice,<sup>1,2</sup> V. Sautter,<sup>4</sup> S. Le Mouélic,<sup>5</sup> R. C. Wiens,<sup>3</sup> C. Fabre,<sup>6</sup> W. Goetz,<sup>7</sup> D. Bish,<sup>8</sup> N. Mangold,<sup>5</sup> B. Ehlmann,<sup>9,10</sup> N. Lanza,<sup>3</sup> A.-M. Harri,<sup>11</sup> R. Anderson,<sup>12</sup> E. Rampe,<sup>13</sup> T. H. McConnochie,<sup>14</sup> P. Pinet,<sup>1,2</sup> D. Blaney,<sup>10</sup> R. Léveillé,<sup>15</sup> D. Archer,<sup>13</sup> B. Barraclough,<sup>16</sup> S. Bender,<sup>16</sup> D. Blake,<sup>17</sup> J. G. Blank,<sup>17</sup> N. Bridges,<sup>18</sup> B. C. Clark,<sup>19</sup> L. DeFlores,<sup>10</sup> D. Delapp,<sup>3</sup> G. Dromart,<sup>20</sup> M. D. Dyar,<sup>21</sup> M. Fisk,<sup>22</sup> B. Gondet,<sup>23</sup> J. Grotzinger,<sup>9</sup> K. Herkenhoff,<sup>12</sup> J. Johnson,<sup>18</sup> J.-L. Lacour,<sup>24</sup> Y. Langevin,<sup>23</sup> L. Leshin,<sup>25</sup> E. Lewin,<sup>26</sup> M. B. Madsen,<sup>27</sup> N. Melikechi,<sup>28</sup> A. Mezzacappa,<sup>28</sup> M. A. Mischna,<sup>10</sup> J. E. Moores,<sup>29</sup> H. Newsom,<sup>30</sup> A. Ollila,<sup>30</sup> R. Perez,<sup>31</sup> N. Renno,<sup>32</sup> J.-B. Sirven,<sup>24</sup> R. Tokar,<sup>16</sup> M. de la Torre,<sup>9</sup> L. d'Uston,<sup>1,2</sup> D. Vaniman,<sup>16</sup> A. Yingst,<sup>16</sup> MSL Science Team†

The ChemCam instrument, which provides insight into martian soil chemistry at the submillimeter scale, identified two principal soil types along the Curiosity rover traverse: a fine-grained mafic type and a locally derived, coarse-grained felsic type. The mafic soil component is representative of widespread martian soils and is similar in composition to the martian dust. It possesses a ubiquitous hydrogen signature in ChemCam spectra, corresponding to the hydration of the amorphous phases found in the soil by the CheMin instrument. This hydration likely accounts for an important fraction of the global hydration of the surface seen by previous orbital measurements. ChemCam analyses did not reveal any significant exchange of water vapor between the regolith and the atmosphere. These observations provide constraints on the nature of the amorphous phases and their hydration.

The composition, mineralogy, and volatile inventory of the martian soil constitute an open record of the igneous history of the martian crust, its meteoritic bombardment, and the physical and chemical weathering processes that transformed primary igneous rocks into secondary products [e.g., (1–3)]. They reflect the aqueous history of Mars and the evolution of its climate. Physical weathering, transport, and sorting processes have redistributed crustal constituents in the soil, thus making its composition difficult to decipher by remote sensing observations. However, these processes also make the crust composition accessible through local in situ measurements.

From orbital observations (neutron, gamma-ray, and near-infrared spectroscopy), the martian surface is known to hold 2 to ~10 weight percent (wt %) of water-equivalent hydrogen at mid- and low latitudes (4–6). Thermodynamic models of ice stability [e.g., (7)] and equilibration models of various hydrous minerals [e.g., (8, 9)] have ruled out some simple explanations for the origin of this water reservoir. Although hydrated sulfates and clay minerals have been detected from orbit, they cover only a small fraction of the entire surface (10–12) and, to the extent of what can be observed by remote sensing, are limited to bedrock outcrops (13, 14), whereas the hydration of the topmost microns of the regolith probed by the Visible and Infrared Mineralogical Mapping Spectrometer (OMEGA) aboard the European Space Agency's Mars Express orbiter is

global and usually unrelated to bedrock exposures (6, 15). Therefore, the nature and origin of this global hydration remain largely unknown. Determining its nature is important for understanding the relationship between the regolith and the atmosphere as well as the aqueous history of Mars overall.

Before the Mars Science Laboratory mission, the bulk chemical composition of the soil was characterized in situ at five different locations on Mars by Viking 1 and 2 (16, 17), Mars Pathfinder (18), and the Mars Exploration Rovers (MERs) both at Meridiani Planum (19) and in Gusev Crater (20). Both bright dust and dark soil deposits on opposite sides of the planet were found to be very similar (21). The Gamma Ray Spectrometer (GRS) onboard the Mars Odyssey orbiter provided data about the elemental composition of the martian surface (4) and revealed large-scale heterogeneities, suggesting both local and regional sources for the surficial materials (22). Analyses of martian meteorites gave detailed information on the composition of the martian crust and interior (23). The composition of the martian surface was also estimated indirectly from its mineralogical characterization (24–26), but the cross section for very fine particles in these observations is often inordinately small. These investigations covered very different spatial scales, but no in situ information on martian soil chemistry was available at the subcentimeter scale (in areal extent), except for its volatile inventory in organic and volatile inorganic compounds by the

Viking and Phoenix landers (~100-mg samples were analyzed by the Viking Molecular Analysis Experiment) (27, 28). This higher resolution is crucial to unraveling the chemical and physical processes that formed the martian soil. Understanding the soil fine-scale chemistry, including its hydration, is an important objective of the ChemCam instrument onboard the Curiosity rover.

The laser-induced breakdown spectrometer (LIBS) on the ChemCam instrument (29, 30) provides insight on martian soil and dust chemical variability at the submillimeter scale. The small sampling area of the ChemCam laser (~350 to 550  $\mu\text{m}$  depending on distance) allows it to isolate various soil components and identify mixing trends that bulk measurements might average together. The spectroscopic measurement of each individual soil, or “LIBS point” (31), is typically obtained from a series of 30 to 50 laser shots. Because each shot produces a LIBS spectrum of a deeper portion of the soil than the previous shot, it is possible to retrieve a profile of chemical composition to depths of a few millimeters in soils and a few tens of micrometers in rocks. The uncertainty budget of the LIBS measurements is small enough for such types of analyses to be performed. This yields analyses deeper than the probing depth of thermal, near-infrared, and x-ray spectrometers but shallower than GRS

<sup>1</sup>Université de Toulouse, UPS-OMP, IRAP, 31028 Toulouse, France. <sup>2</sup>CNRS, IRAP, 9 Av. Colonel Roche, BP 44346, F-31028 Toulouse cedex 4, France. <sup>3</sup>Los Alamos National Laboratory, Los Alamos, NM 87545, USA. <sup>4</sup>Muséum National d'Histoire Naturelle, Laboratoire de Minéralogie et Cosmochimie du Muséum, 75005 Paris, France. <sup>5</sup>LPGN, CNRS, UMR6112, Université Nantes, 44322 Nantes, France. <sup>6</sup>GeoRessources, CNRS, UMR7356, Université de Lorraine, 54506 Vandoeuvre les Nancy, France. <sup>7</sup>Max Planck Institut für Sonnensystemforschung, 37191 Katlenburg-Lindau, Germany. <sup>8</sup>Indiana University, Bloomington, IN 47405, USA. <sup>9</sup>California Institute of Technology, Pasadena, CA 91125, USA. <sup>10</sup>Jet Propulsion Laboratory, California Institute of Technology, Pasadena, CA 91109, USA. <sup>11</sup>Earth Observation Research Division, Finnish Meteorological Institute, 00101 Helsinki, Finland. <sup>12</sup>U.S. Geological Survey, Astrogeology Science Center, Flagstaff, AZ 86001, USA. <sup>13</sup>NASA Johnson Space Center, Houston, TX 77058, USA. <sup>14</sup>University of Maryland, College Park, MD 20740, USA. <sup>15</sup>Canadian Space Agency, Saint-Hubert, Quebec J3Y 8Y9, Canada. <sup>16</sup>Planetary Science Institute, Tucson, AZ 85719, USA. <sup>17</sup>NASA Ames Research Center, Moffett Field, CA 94035, USA. <sup>18</sup>Applied Physics Laboratory, Johns Hopkins University, Laurel, MD 20723, USA. <sup>19</sup>Space Science Institute, Boulder, CO 80301, USA. <sup>20</sup>ENS, 69007 Lyon, France. <sup>21</sup>Mount Holyoke College, South Hadley, MA 01075, USA. <sup>22</sup>Oregon State University, Corvallis, OR 97331, USA. <sup>23</sup>Institut d'Astrophysique Spatiale, 91405 Orsay, France. <sup>24</sup>Commissariat à l'Énergie Atomique et aux Énergies Alternatives, Centre de Saclay, 91400 Gif-sur-Yvette, France. <sup>25</sup>Rensselaer Polytechnic Institute, Troy, NY 12180, USA. <sup>26</sup>ISTerre, 38041 Grenoble, France. <sup>27</sup>Niels Bohr Institute, University of Copenhagen, 2100 Copenhagen, Denmark. <sup>28</sup>Optical Science Center for Applied Research, Delaware State University, Dover, DE 19901, USA. <sup>29</sup>Center for Research in Earth and Space Science, York University, Toronto, Ontario M3J 1P3, Canada. <sup>30</sup>University of New Mexico, Albuquerque, NM 87131, USA. <sup>31</sup>Centre National d'Études Spatiales, 31400 Toulouse, France. <sup>32</sup>Department of Atmospheric, Oceanic and Space Science, University of Michigan, Ann Arbor, MI 48109, USA.

\*Corresponding author. E-mail: pmeslin@irap.omp.eu

†MSL Science Team authors and affiliations are listed in the supplementary materials.

# Curiosity at Gale Crater

nuclear techniques, which can profile a few tens of centimeters. ChemCam is sensitive to the presence of hydrogen and can therefore investigate its spatial and temporal variability, providing constraints on the H<sub>2</sub>O budget of the martian surface.

## Results

With 139 LIBS points acquired on soil targets during the first 90 sols of the mission (~3600 spectra) (Fig. 1A), ChemCam has collected a data set that is well suited to statistical analysis. Here, a soil target is defined as a loose, unconsolidated material that can be distinguished from rocks, bedrock, or strongly cohesive sediments (32). Images taken with the Remote Microscopic Imager (RMI) show a diversity of soil targets analyzed by ChemCam that range from homogeneous soils made of fine-sand particles (Fig.

1C) to mixtures of fines and pebbles with typical grain sizes of <4 mm, classified as “fine gravels” in terms of the Wentworth-Krumbein scale (Fig. 1, B and D).

## Soil Chemical Diversity

A cluster analysis of the spectra based on an independent components analysis (ICA) (33, 34) and chemical quantification obtained with a partial least-squares technique known as PLS2 (34–36) revealed that the soils observed during the first 90 sols at Gale crater follow a compositional trend between two major end members: a mafic component (cluster 1 or “mafic type”), and an alkali-, aluminum-, and silica-rich component (cluster 2 or “felsic type”). Cluster analysis reveals that two main groups of targets are indeed discriminated by their Si, Al, and Na components (Fig. 2 and Fig. 3A). Compositions obtained with PLS2 are

consistent with this analysis (Fig. 3B). A third cluster shares a relatively high Mg component with the mafic type but has a lower H and a higher Na component. Its composition is intermediate between the two former end members. The mean composition of cluster 1 is close to the APXS (Alpha Particle X-ray Spectrometer) composition of Portage (a soil target in a rover wheel scuff measured by both instruments) and to the composition of the dust measured by ChemCam on rock surfaces, although the latter was found to show less chemical variation (Table 1) (37). The felsic type is similar in composition to the high-Si minerals measured by ChemCam in neighboring rocks, such as Stark, a pitted, pumice-like rock, and Link, classified as a fine-pebble fluvial conglomerate (Fig. 3B) (38–40). Felsic-type soil targets are mostly found in the hummocky region in the vicinity of the landing site (Bradbury Rise)

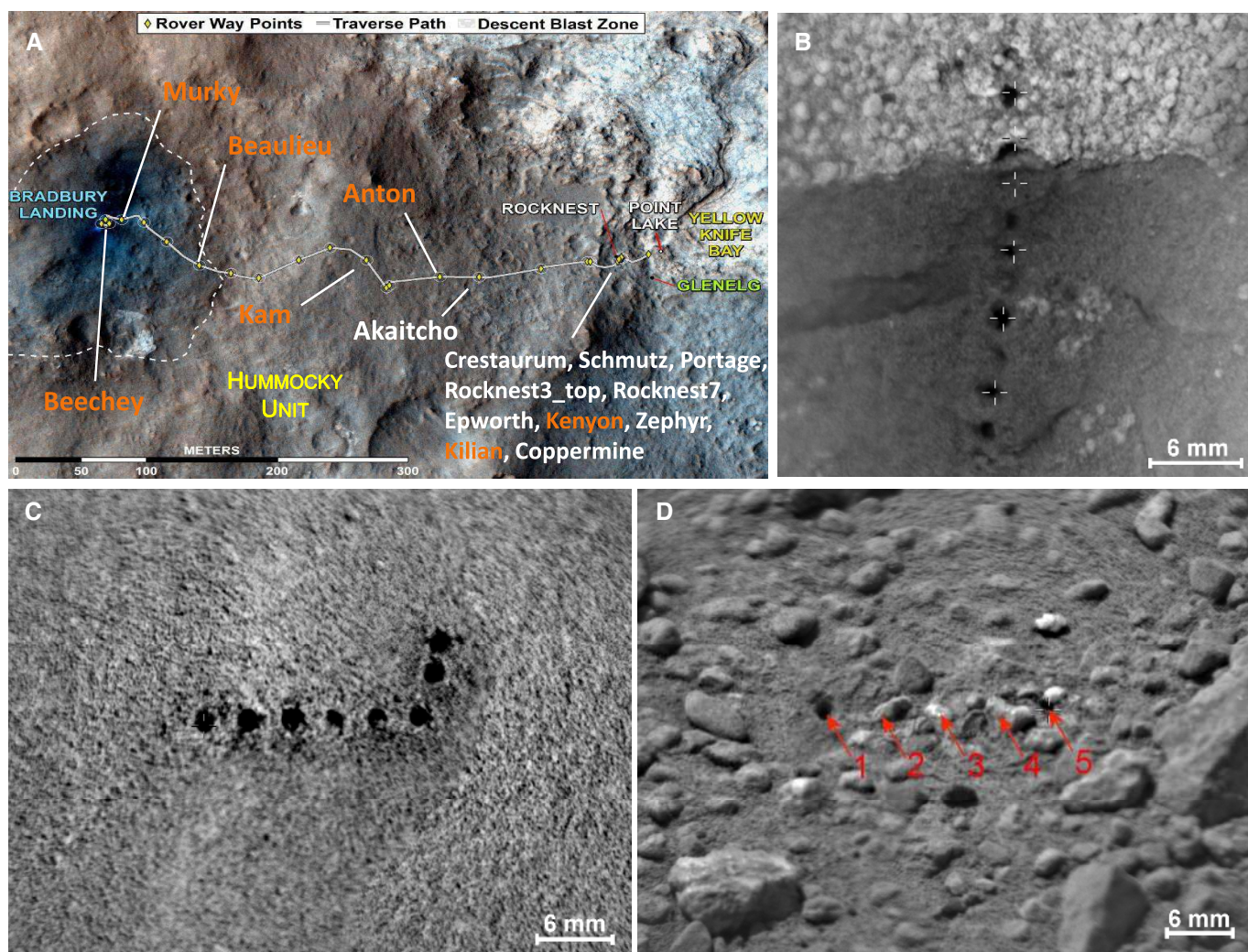


**Fig. 1. ChemCam soil targets.** (A) Rover traverse and location of ChemCam soil targets for the first 100 sols [image credit: NASA/JPL-Caltech/Univ. of Arizona]. Names appearing in orange correspond to locations where ChemCam points belonging to cluster 2 (felsic type) were found. Points belonging to cluster 1 (mafic type) were found in all locations. (B to D) Three examples of soil targets imaged by the RMI: (B) vertical transect across a trench dug into the Rocknest sand shadow, covered with ~1-mm grains (Epworth3, sol 84); 15 ChemCam points were acquired

from the bottom to the center of the image; the cross hairs only represent some of the LIBS spots; (C) homogeneous, fine-grained soil (Crestaurum, sol 83); (D) heterogeneous soil containing ~3-mm pebbles (Beaulieu, sol 33). The eight points of target Crestaurum and Beaulieu point #1 belong to cluster 1. Beaulieu points #2, #3, and #4 belong to cluster 2. Beaulieu point #5, at the intersection between a small pebble and the surrounding fines, belongs to cluster 3. Some points of Epworth, on top of the Rocknest sand shadow (B), also belong to cluster 3.

(Fig. 1A), which reveals a change in local source composition along the traverse. The composition of the average martian soil measured by other in situ missions (41) falls near the center of the Gale crater soil data cluster (Fig. 3B), closer to the mafic type, consistent with Mars Odyssey GRS data measured in these locations (22).

### Relation Between Grain Size and Composition

Integrating physical properties such as grain size with chemical data is important to better understand the soil composition and its formation processes (3). Analyses of ChemCam RMI images and variations of chemical composition and intensity of the spectra with depth (fig. S1) (34) reveal a correlation between composition and grain size. The mafic-type soils comprise a mixture of grains that are both coarser and finer than the LIBS spot size of  $\sim 400\ \mu\text{m}$  (42), the coarser grains having on average higher  $\text{SiO}_2$  and alkali abundances (Fig. 3B and fig. S3). Conversely, the felsic-type targets are almost exclusively coarse, millimeter-sized grains. This explains why cluster 2 is classified with some rock targets in the cluster analysis (Fig. 3A). The observed compositional trend, almost continuous, and its spread (Fig. 3B) could be produced by the mechanical mixing of different proportions of the two former components, from solid solutions or mixing between subcategories of each cluster, or from the presence of other chemical extremes falling on the same trend that could only be revealed by classification at the subpoint scale. Part of the spread

can also result from the inherent shot-to-shot dispersion of the spectra. Cluster 3 is an intermediate category of targets that is more difficult to define uniquely, probably as a result of the above processes and because the sorting of grains is less obvious. In some instances, clear mechanical mixing between the mafic and felsic types can be seen on RMI images of cluster 3 targets (Fig. 1D) or by looking at profiles of chemical composition with depth, which reveals the presence of buried coarse felsic grains (e.g., Epworth2 #3, located in the sand shadow armor shown in Fig. 1B).

### Chemical Variability at Rocknest Site

The Curiosity rover remained for  $\sim 45$  sols at a site called Rocknest in the vicinity of an aeolian bedform. The Rocknest soils, mostly sampled in the sand shadow, belong almost entirely to cluster 1. They differ distinctly from the iron-rich mafic rocks identified at Rocknest and are characterized by higher  $\text{Mg}/(\text{Mn,Cr})$  (43), H, and Ca ICA components and lower Fe and Ti components than the latter (Fig. 3, A and C). The positive correlation between Mg and Cr suggests that they contain various proportions of picritic basaltic material. Although Mn and Cr are positively correlated with Mg in Rocknest soils, their concentration is lower than in the Rocknest rocks. These differences suggest an absence of a genetic relationship between soils and rocks in this area, except as noted below.

Spatial chemical diversity as a result of physical sorting by grain size (44) was readily appar-

ent in the sand shadow. Analysis points obtained on top of the bedform, armored with millimeter-sized grains (Fig. 1B), have on average higher Si, Na, K, and Al contents than the interior of the trench dug into the sand shadow, which is composed of fine-sand particles (fig. S3) (34). However, none of these points is classified with either felsic rocks/soils or Rocknest rocks, except Kenyon #8 (cluster 2) and Epworth2 #3 (classified in cluster 3 as a result of mixing between mafic type and felsic type), which suggests that they are not locally derived and have been subject to transport. The presence of the coarse grains Kenyon #8 and Epworth2 #3 provides evidence, however, that some local material has been incorporated into or on top of the sand shadow.

### Low $\text{SiO}_2$ Abundances in the Fine-Grained Component

Some points within the mafic type (cluster 1), particularly its fine-grained fraction, have low  $\text{SiO}_2$  (as low as  $\sim 34$  wt %) and a low sum of predicted oxides (Fig. 3B), averaging from  $\sim 87$  wt % totals for the cluster 1 average composition to as low as  $\sim 76$  wt % totals for the low  $\text{SiO}_2$  value points. This suggests that the mafic-type soils contain a greater abundance of several elements (H, C, N, P, S, Cl, F) that are not easily detected by LIBS or quantifiable by PLS2. The low  $\text{SiO}_2$  and total values may be attributed to the presence of an amorphous component that has been detected in the soil by CheMin and quantified by CheMin and APXS at levels of 27 to 45 wt % (45, 46). This component is Si-poor ( $\text{SiO}_2 = 37.2$  wt %) and S-, Cl-, and possibly P-rich (with values of  $\text{SO}_3 = 11.0$  wt %,  $\text{Cl} = 1.4$  wt %, and  $\text{P}_2\text{O}_5 = 2.1$  wt %) (46). Adding this composition from CheMin/APXS and 5 to 9 wt % of  $\text{H}_2\text{O}$  inferred from SAM (Sample Analysis at Mars) for the amorphous component (47) to the initial ChemCam totals yields a sum of  $\sim 97.5$  wt % for the low-silica samples—a reasonable total given the accuracy of the PLS2 method (48) and the omission of other minor oxides in the calculation. It is also possible that lower  $\text{SiO}_2$  values are associated with even greater abundances of S, Cl, and P than derived from the bulk values calculated or measured by CheMin and APXS. This analysis suggests that ChemCam has probed the soil amorphous component incorporated in the mafic type, which was made possible by the small area of the LIBS interaction.

It is also noteworthy that the fine-grained targets belonging to cluster 1 have higher CaO concentrations. PLS2 results reveal an anticorrelation between CaO and  $\text{SiO}_2$  that mimics that between  $\text{SiO}_2$  and the sum of missing oxides (Fig. 4), implying that a fraction of CaO is associated with an element that is not predicted by the PLS2 technique (49, 50). Some of this calcium could be associated with sulfur, which may be evidence for incorporation of Ca sulfates from neighboring areas. SAM and CheMin instruments have not found evidence for abundant crystalline Ca sulfate minerals in Rocknest soil ( $<150\ \mu\text{m}$  fraction),

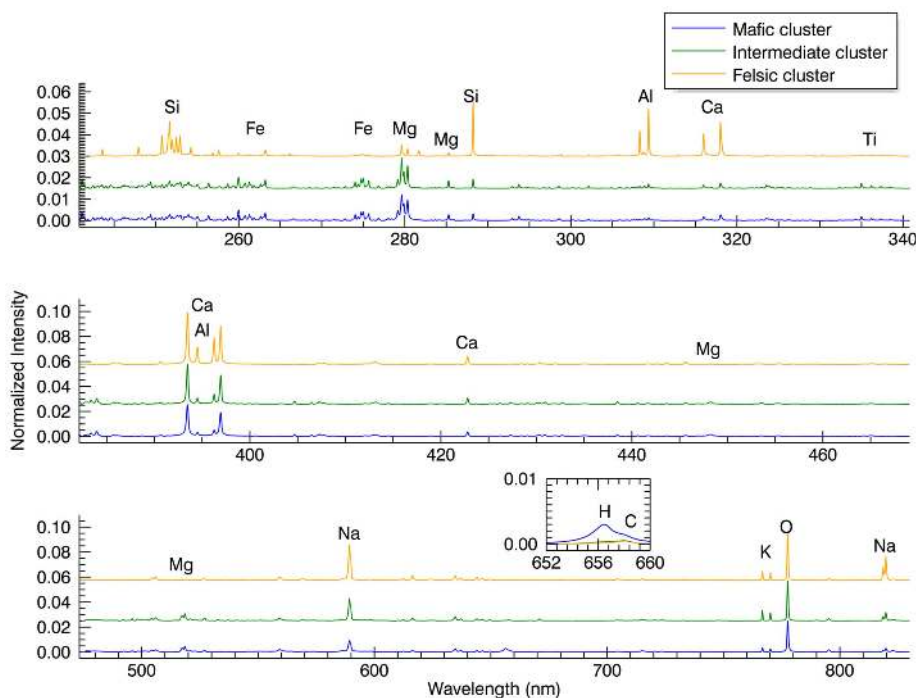


**Fig. 2. Characteristic spectra of the three clusters.** LIBS spectra of points Beaulieu #1 (mafic type), Beaulieu #2 (felsic type), and Beaulieu #5 (intermediate cluster), also shown in Fig. 1D. Each row corresponds to one of the three channels of ChemCam's Body Unit. An offset has been applied to separate the three spectra. The inset shows the hydrogen and carbon lines around 656 nm.

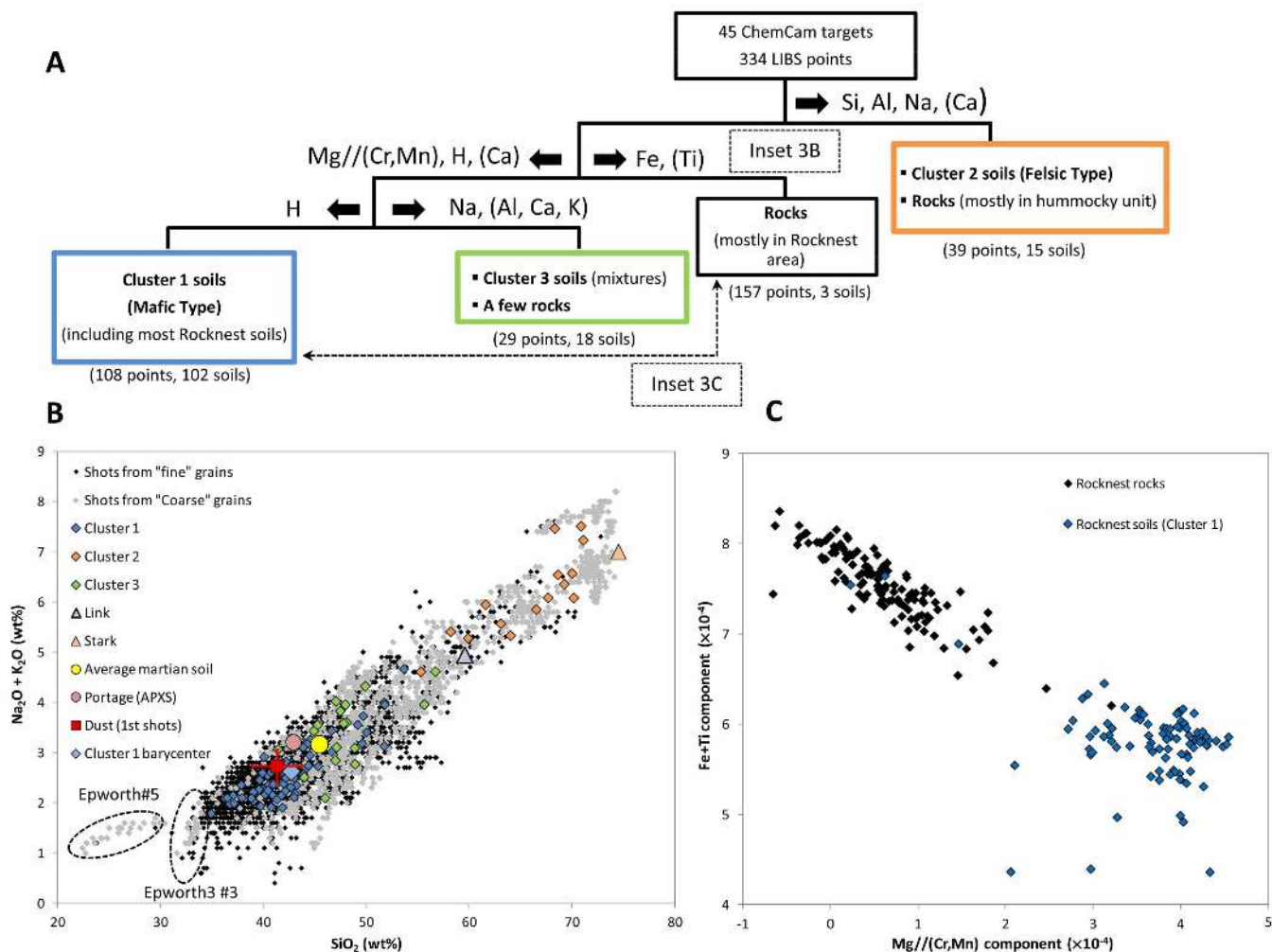


**Fig. 3. Classification of ChemCam targets and chemical trends.** (A) Schematic dendrogram of the clustering analysis of ChemCam targets (rocks and soils), based on ICA. The elements driving the division of the clusters are listed on each branch. The elements appearing in parentheses, although not sufficient to divide the clusters, show significantly larger signal than the mean of the whole population or subgroup. (B) Composition of ChemCam soil targets (the averages of each LIBS point are represented by colored diamonds), Link and Stark rocks, and dust, derived from the PLS2 technique. The dust composition is shown with  $\pm 1\sigma$  standard deviation. All shot-by-shot data are

also shown, divided between shots that qualitatively appear to be from "coarse" grains (in gray) and from "fine" grains (in black). The average martian soil composition from (41) and the APXS composition of soil Portage (46) are shown for comparison. Differences in normalization are described in the supplementary material (34). (C) ICA classification of soils and rocks measured at Rocknest site showing a clear distinction between them along the (Fe+Ti) and Mg/(Cr,Mn) components (43). The point Epworth #5 (B), which represents a class in itself (characterized by its CaO component), is not represented in the dendrogram for the sake of clarity. Epworth3 #3 is another calcium-rich coarse grain.

although CheMin reports 1.4 wt % anhydrite, which is near its detection limits (45, 47). Ca perchlorates were identified tentatively by SAM at abundances below the detection limit of CheMin (45, 47). The largest CaO and lowest SiO<sub>2</sub> values were obtained for points Epworth #5 and Epworth3 #3 (Fig. 4), two coarse grains buried in the Rocknest sand shadow, whose size (>150 μm) probably excluded them from being analyzed by SAM and CheMin.

#### Soil Hydration

An outstanding feature in ChemCam LIBS spectra of all cluster 1 soils is a ubiquitous hydrogen emission peak. ICA analysis reveals a hydration trend that closely follows the trend in composition and grain size (Fig. 5). The fine-grained mafic soil component and the dust (Fig. 6A) are

enriched significantly in H relative to the felsic-type component and coarse grains, whose H signal is similar to that of local rocks and ChemCam anhydrous calibration targets (Fig. 5 and Fig. 6A). This trend is consistent with the hypothesis that soils are a mechanical mixture of components characterized by different levels of hydration and that the average hydrogen abundance present corresponds to the proportion of the fine-grained component in the soil.

There are multiple potential carriers for this hydrogen: (i) adsorbed atmospheric H<sub>2</sub>O, controlled by the soil specific surface area (SSA) and possibly forming thin grain-surface brines (51); (ii) hydrated crystalline minerals, including phyllosilicates and salts; and (iii) amorphous or poorly crystalline hydrated phases. CheMin found no

evidence for the presence of hydrated crystalline minerals in the soil, which suggests that the hydrogen detected by ChemCam and H<sub>2</sub>O measured by SAM (47) is either adsorbed or corresponds to the hydration of the amorphous component detected by CheMin, or both. Adsorbed water would be preferentially associated with the amorphous phase if it is porous.

Three experiments were conducted with ChemCam to provide additional constraints on the nature of the observed hydrogen. The variability of hydrogen in the martian soil was monitored as a function of time and depth at different scales: (i) an examination of day/night H variations in the upper millimeter of undisturbed soil; (ii) observations of H variations with depth, over the first millimeter and over a few centi-

**Table 1. Soils and dust composition and comparison to previous investigations.** PLS2 mean compositions of clusters 1 and 2 (with standard deviations in parenthesis), dust (ChemCam first shots) (37), and comparison to the average martian soil (41) and to the APXS composition of Portage (46). PLS2 root-mean-square error of prediction (RMSEP) for each element is indicated in the rightmost

	Cluster 1 (mean)	Average martian soil*	Portage soil (ChemCam)	Portage soil (APXS)	Dust (ChemCam)	Dust (MER APXS)†	Cluster 2 (mean)	PLS2 RMSEP
SiO <sub>2</sub>	43.5 (3.8)	45.41	45.0 (4.4)	42.88 ± 0.47	42.0 (2.4)	44.84 ± 0.52	66.0 (5.0)	7.3
TiO <sub>2</sub>	0.6 (0.2)	0.90	0.6 (0.2)	1.19 ± 0.03	0.8 (0.2)	0.95 ± 0.08	0.1 (0.1)	0.7
Al <sub>2</sub> O <sub>3</sub>	11.4 (1.1)	9.71	11.9 (1.4)	9.43 ± 0.14	10.9 (0.8)	9.32 ± 0.18	11.6 (1.6)	3.0
FeO <sub>T</sub>	13.8 (1.1)	16.73	13.6 (1.5)	19.19 ± 0.12	13.7 (1.1)	16.96‡ ± 0.74	6.2 (3.7)	5.7
MgO	7.5 (1.5)	8.35	7.8 (1.8)	8.69 ± 0.14	7.3 (0.8)	7.89 ± 0.32	1.4 (1.1)	4.0
CaO	8.0 (1.4)	6.37	7.7 (1.8)	7.28 ± 0.07	7.8 (1.1)	6.34 ± 0.20	7.5 (2.7)	4.2
Na <sub>2</sub> O	2.2 (0.4)	2.73	2.3 (0.5)	2.72 ± 0.10	2.0 (0.3)	2.56 ± 0.33	4.0 (0.4)	0.8
K <sub>2</sub> O	0.6 (0.2)	0.44	0.6 (0.2)	0.49 ± 0.01	0.7 (0.2)	0.48 ± 0.07	2.1 (0.5)	0.9
Cr <sub>2</sub> O <sub>3</sub>	—	0.36	—	0.49 ± 0.02	—	0.32 ± 0.04	—	—
MnO	—	0.33	—	0.41 ± 0.01	—	0.33 ± 0.02	—	—
P <sub>2</sub> O <sub>5</sub>	—	0.83	—	0.94 ± 0.03	—	0.92 ± 0.09	—	—
SO <sub>3</sub>	—	6.16	—	5.45 ± 0.10	—	7.42 ± 0.13	—	—
Cl	—	0.68	—	0.69 ± 0.02	—	0.83 ± 0.05	—	—
Sum of oxides not quantified by PLS2		8.36		7.98		9.82		
Residual§	-3.0		-2.4		-4.2			
Total	87.6	99	89.5	99.85	85.2	99.2	98.9	11.4

\*From (41). †From (54). ‡FeO = 10.42 ± 0.11 wt %, Fe<sub>2</sub>O<sub>3</sub> = 7.28 ± 0.70 wt %. §Difference, expressed as [(total APXS) - (sum of oxides not quantified)] - (total PLS2), between adjacent columns. This residual is partly due to the difference of normalization, as APXS data are normalized on a water- and carbon-free basis (34).

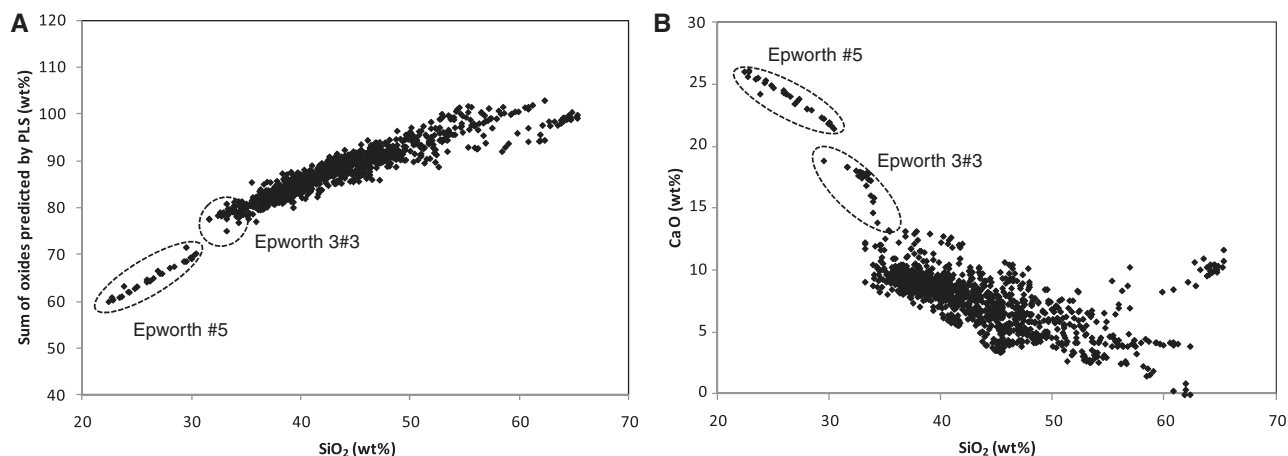


**Fig. 4. Chemical correlations in the Rocknest soil.** (A) Correlations between the sum of missing oxides and SiO<sub>2</sub>, suggesting that the low SiO<sub>2</sub> values are associated with missing elements. (B) Anticorrelation between CaO and

SiO<sub>2</sub>. Shot-by-shot PLS2 values of Rocknest soil are plotted together with shots from Epworth #5 and Epworth3 #3, two coarse grains found on top of and in the interior of the sand shadow, showing relatively large CaO abundances.

eters, when a scoop in the Rocknest sand shadow was excavated; and (iii) observations of H variations with time, over a few days, of a freshly exposed soil to look for signs of desiccation. The first experiment was performed on a fine-grained soil target, Crestaurum (Fig. 1C), at the surface of an aeolian bedform. Day and pre-dawn measurements of H showed very consistent values and no H enrichment in the first shots, which are most likely to be affected by diurnal exchange of H<sub>2</sub>O or frost deposit (Fig. 6A). The second experiment was performed on a large set of points, both in undisturbed soil and in the interior of the ~3-cm-

deep trench in the Rocknest sand shadow; no statistically significant variations were seen within the first millimeter probed or between the different points (Fig. 6, B and D). This suggests that the H<sub>2</sub>O content measured by SAM may be extrapolated to the surface of similar undisturbed soils. In the third experiment, similar points within the interior of the trench monitored over a 25-sol period, 11 sols after the soil was exposed, did not reveal statistically significant variations (Fig. 6C). These results, together with preliminary estimates of the sensitivity of ChemCam measurements (52), suggest that the diurnal exchange of H<sub>2</sub>O with the atmosphere

leads to variations of H<sub>2</sub>O abundance of less than ~1.1 wt % for the type of soils we analyzed under humidity conditions prevailing at Gale crater near solar longitude L<sub>s</sub> ~ 200°. Either the equilibration of the interior of the sand shadow with the surface atmosphere occurred faster than 11 sols, or the gradient of water-equivalent hydrogen with depth was less than ~0.25 wt % over a few centimeters.

## Discussion

### Origin of the Soils

The abundance and distribution of light-toned pebbles with high Si, Na, and Al contents along

# Curiosity at Gale Crater

the rover traverse suggest that material with felsic composition is common near the landing site but limited to the pre-Rocknest hummocky unit. The surface of Bradbury Rise is characterized by the presence of fluvial sedimentary conglomerates, only one of which (Link) was observed by ChemCam (39). Its clasts have a range of SiO<sub>2</sub>, Al<sub>2</sub>O<sub>3</sub>, and alkali compositions close to that of alkali feldspar (38–40), consistent with the composition of some felsic-type pebbles. This observation supports the interpretation that loose and cemented clasts in the hummocky region have a common origin. In this case, the felsic-type pebbles would have one of two origins: They could have resulted from in situ weathering of the sedimentary conglomerates, or they could have been transported and deposited from the same source region without being cemented. The abundance of such pebbles reinforces the view that the hummocky unit could contain abundant feldspar-rich crustal material that has not been probed by past instruments (38, 40) and possibly originates from the crater rim (39). The pebbles with largest SiO<sub>2</sub> concentrations may represent lithic fragments from silica-rich, pumice-like rocks similar to Stark (38, 40).

The mafic soil component was found not only in the Rocknest sand shadow and in aeolian bedforms, but throughout the rover traverse (Fig. 1A). It differs chemically from any of the rocks analyzed in the hummocky unit, supporting the idea that it is not locally derived at the scale of this geological unit. Its composition is similar to that of soils and dust measured elsewhere on Mars. Its presence in soils at Gale crater must reflect the efficiency of large-scale processes such as aeolian transport and impact gardening. It could reflect the widespread presence of regions with similar basaltic composition, possibly characterized by lower resistivity to physical and chemical weathering. On the other hand, investigations at other landing sites also found relatively little influence from local bedrock composition (21), rock compositions found at Gale crater differ from other sites (38), and Mars Odyssey GRS found large provinces characterized by different compositions (22, 53); these findings could indicate that the mafic soil component in fact represents an average of different compositions as a result of large-scale homogenization processes. It was suggested, for instance, that this ubiquitous material was made of two unrelated components: a component derived from relatively young olivine-rich basalts degraded under relatively anhydrous conditions and a component containing clay minerals, amorphous silica, and sulfur- and chlorine-rich nanophase ferric oxides resulting from the alteration of ancient rocks under hydrous conditions (2). This type of scenario could be consistent with ChemMin characterization of the Rocknest soil [although ChemMin did not detect the presence of phyllosilicates in that soil (45)] and with the evidence for the presence of a hydrated amorphous component.

The dust analyzed by ChemCam is basaltic, and its composition is similar to that measured by the MER APXS at the surface of bright soils (54

(Table 1). Both its composition (including an SiO<sub>2</sub> abundance greater than that of the amorphous component) and its chemical homogeneity (i.e., small point-to-point variability, reflected in a standard deviation lower than that of cluster 1) suggest that its chemical alteration was limited, in agreement with previous observations of the presence of olivine minerals by the MERs (54–56). Fine by-products of the physical weathering of larger basaltic grains during their transport (57), or aeolian abrasion of rocks, would be consistent with these observations. On the other hand, the hydration measured by ChemCam, and the high S, P, and Cl content probably associated with nanophase iron oxides inferred from MER APXS analysis (54, 55), hint at the presence of weathering products, although adsorption could also play an important role given their small size. The homogeneity of the dust composition observed by ChemCam could therefore also reflect the very small scale of the dust particles with respect to the size of the LIBS spot.

The fact that none of the points analyzed on the Rocknest bedform armor is classified with Rocknest or Bradbury Rise rocks (except Kenyon #8) suggests that the millimeter-sized pebbles traveled some distance from another source region before ending their course at Rocknest. This is consistent with their subangular to subrounded shape, which is indicative of the mechanical erosion they have undergone (fig. S2).

## Hydration of the Amorphous Phase and Specific Surface Area of the Soil

Although the nature of the amorphous component detected by ChemMin in the <150- $\mu$ m fraction of the Rocknest soil remains unclear, its x-ray diffraction pattern resembles that of basaltic glass with some allophane, a short-range ordered hydrous aluminosilicate (45). Chemical data, however, suggest that the latter is likely a surrogate for Fe<sup>3+</sup>-bearing amorphous phases, such as Fe-allophane, hisingerite (58), or nanophase iron oxides (45, 46). Interpretations of orbital data also suggest the presence of allophane-like silicate phases and ferrihydrite at the surface of Mars (26, 59, 60), although Al-rich allophane is not consistent with APXS chemical data (46) and requires conditions of moderate pH ( $\geq 5$ ) to form (61).

The large fraction of poorly ordered ferric materials and their association with hydrogen and other volatile species suggest a similarity to terrestrial andisols. These soils develop in volcanic ejecta (such as volcanic ash, pumice, or cinders) and/or in volcanoclastic materials usually rich in volcanic glass; they are characterized by a colloidal fraction dominated by short-range ordered minerals or noncrystalline phases, especially allophane, imogolite, and noncrystalline oxyhydroxides (e.g., ferrihydrite), or Al/Fe-humus complexes often together with opaline silica (61, 62). The strong sorption capacity of andisols

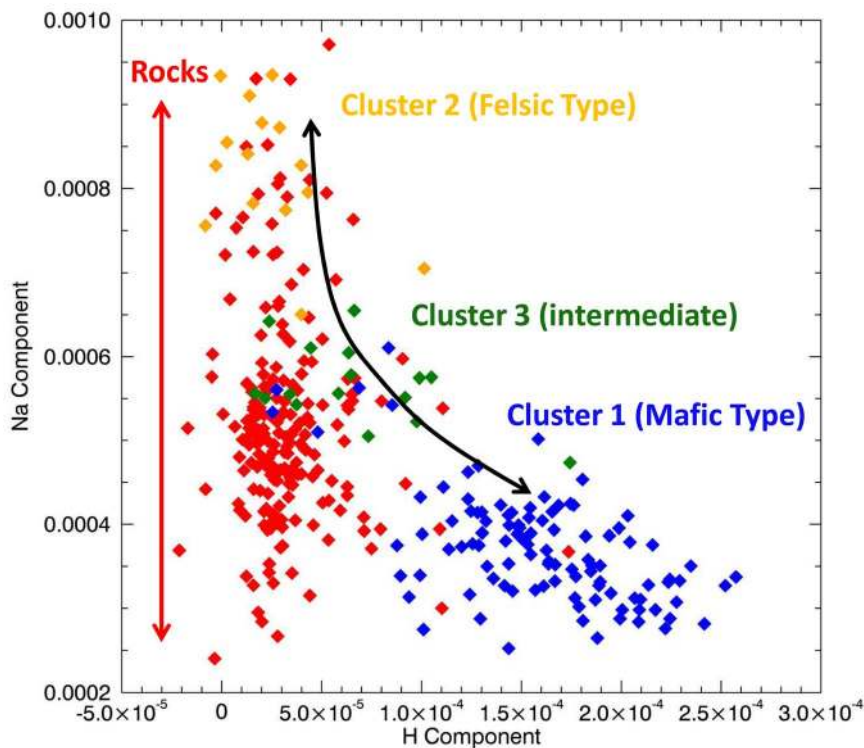


**Fig. 5. ICA classification of soils and rocks along Na and H components.** A hydration trend from cluster 2 to cluster 1 soils and going through cluster 3 is observed, away from the rocks (the x and y axis represent the covariance between each of the spectra and the independent components) (34). It suggests mechanical mixing between fine hydrated particles and drier coarse grains.

due to the presence of these amorphous phases could be relevant to Mars. Sorption of phosphate in andisols, for instance, has been shown to inhibit the crystallization of ferrihydrite to more crystalline goethite and hematite (61). High sorption capacities could also make the regolith an important contributor to the atmospheric H<sub>2</sub>O cycle (63, 64). In andisols, allophane and iron (oxy)hydroxides contain substantial amounts of adsorbed H<sub>2</sub>O because of their large specific surface area (SSA) (65) and the presence of surface hydroxyl groups that act as strong adsorption sites through hydrogen bonding (66). Similarly, the abundance of these hydroxylated phases may dominate the SSA of the martian soil and thus the level of atmospheric H<sub>2</sub>O stored in the regolith. Laboratory experiments per-

formed on ferrihydrite and on phyllosilicate-poor, allophane-rich palagonitic dust from the flanks of Mauna Kea volcano, Hawaii (67, 68), show indeed that these materials can hold relatively large amounts of adsorbed H<sub>2</sub>O (a few wt %) under martian conditions, even at low relative humidities and with relatively fast exchange kinetics (69).

Some differences with the martian soil are therefore unclear. Indeed, the average level of hydration of the amorphous phases (5 to 9 wt %), measured by SAM (47) to a temperature of 835°C, contrasts with the relatively small amount of H<sub>2</sub>O measured at temperatures less than 150° to 200°C, a typical range of temperatures where H<sub>2</sub>O adsorbed in allophane-rich material is released (70). This also contrasts with the lim-

ited time variability of H<sub>2</sub>O abundance measured by ChemCam in the near-subsurface and inferred from orbital observations of the atmospheric water column (71).

Determining the level of regolith-atmosphere exchange of H<sub>2</sub>O, and thus its SSA, is also important to understand why the D/H ratio of soils, measured by SAM, is close to atmospheric values (26). Estimates of the SSA of the martian soil can be deduced from ChemCam day/night experiment results (see Materials and Methods). We find an upper limit for the SSA of the fine-grained component of 30 to 45 m<sup>2</sup> g<sup>-1</sup> (Fig. 7) (34), which does not contradict the only SSA estimate available to date of 17 m<sup>2</sup> g<sup>-1</sup> derived by the Viking Gas Exchange Experiment (72). The relatively low SSA suspected for the

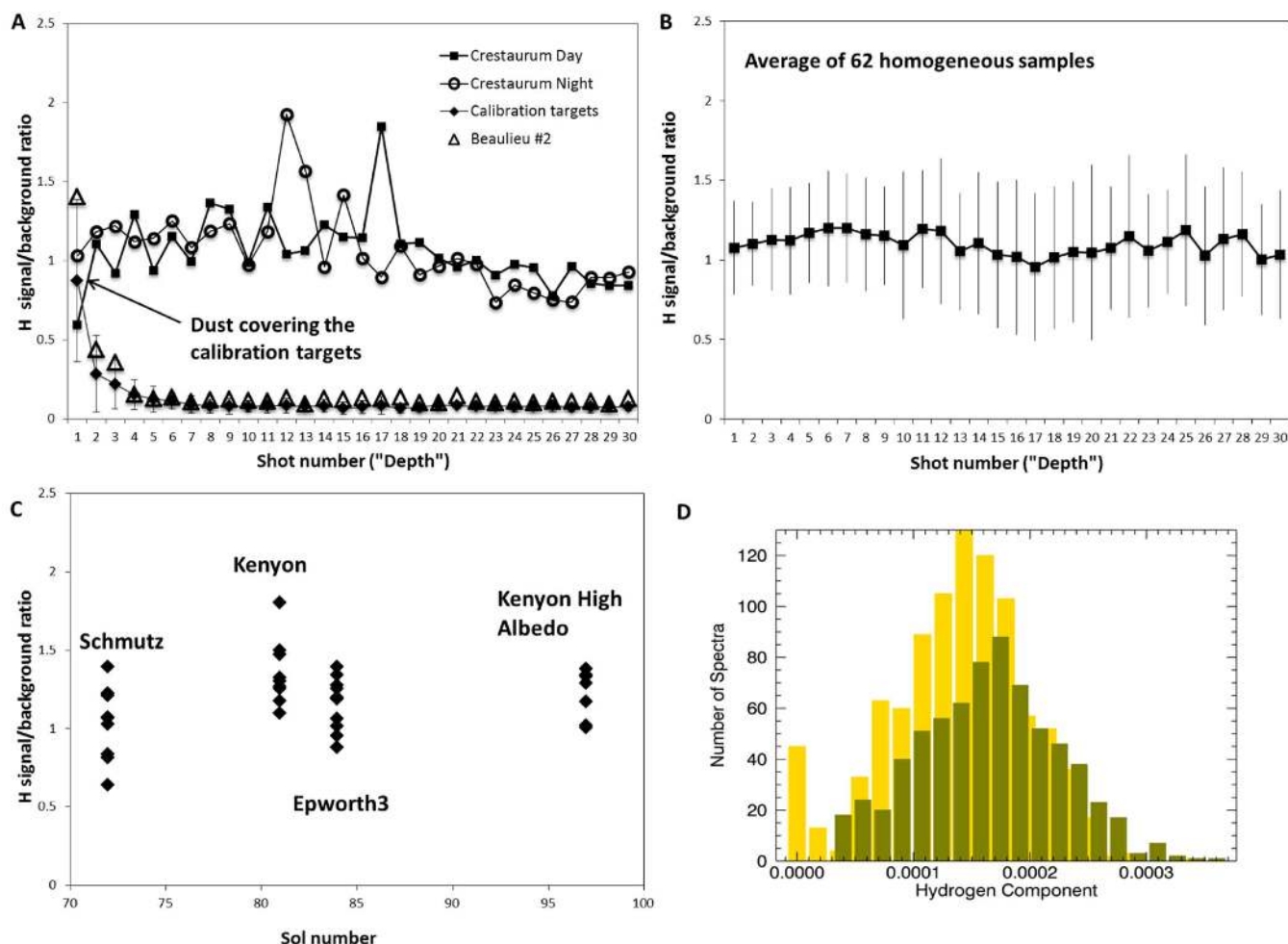


**Fig. 6. Temporal and spatial variability of the hydrogen signal.** (A) Depth profile of the H line intensity (signal to background, S/B) for the Crestaurum target analyzed on sol 74/75 [sol 74, 11:30 a.m. local mean solar time (LMST), and pre-dawn of sol 75, 4:40 a.m. LMST]. The ratio between the mean night and day S/B is 1.003, indicating no sign of water enrichment at night. The average S/B of seven onboard calibration targets, used as a blank, is also displayed. The first five shots reveal the presence of hydrated dust on their surface. The large error bars for these shots are probably due to differences in dust coverage. The H S/B profile of Beaulieu point #2 (Fig. 1D), which belongs to the felsic type, is also shown for comparison. It does not significantly differ

from the blank. (B) Hydrogen S/B ratio over the first 30 shots and averaged over 62 homogeneous, fine-grained samples. Error bars are  $\pm 1\sigma$  (standard deviation of the N averaged samples). (C) Variations of the hydrogen S/B ratio in the interior of the trench as a function of the sol number (the trench was dug on sol 61). Each black point represents the average S/B of one of the LIBS points acquired on the target. The standard deviation around the mean of each target is  $\sim 0.2$ . (D) Histograms of the two populations of spectra acquired in the interior of the trench (green) and in undisturbed surfaces (yellow), and characterized by the same Na component. The x axis represents the H component of the ICA analysis.

noncrystalline fraction of the soil, deduced from the low content of exchangeable H<sub>2</sub>O and compared with the much higher values measured for terrestrial allophane and ferrihydrite, suggests that such strongly hydroxylated silicates may in fact not be a very adequate analog for the martian soil, or that their porous structure has been modified.

### Conclusion

ChemCam and APXS instruments show that the fine-grained soil component measured at Gale crater is likely representative of widespread martian soils, owing to chemical similarity with the soils of other landing sites. It has been sampled not only in undisturbed soils along the rover traverse but also at some depth in Rocknest sand shadow. This component and the dust are found to possess a ubiquitous H emission line in ChemCam spectra. The corresponding hydration, quantified by SAM at Rocknest at a bulk value of ~2.25 wt % (47), relatively consistent with H<sub>2</sub>O abundances of 1 to 3 wt % measured by Viking 1 and 2 (73) and shown by CheMin to be likely carried by amorphous phases (45, 46), could therefore account for an important fraction of the global budget of the water-equivalent hydrogen measured from orbit at mid- and equatorial latitudes by Mars Odyssey GRS and Mars Express OMEGA, in particular the lower limit of ~2 wt % (4–6, 15). Because the hydration of the amorphous component is ~5 to 9 wt % (47), the spatial variations seen from orbit may be part-

ly explained by the presence of different proportions of this hydrated amorphous component in the soil.

### Materials and Methods

#### Constraints on the Specific Surface Area of the Martian Soil at Gale Crater

The SSA of a soil is the primary parameter that controls the amount of H<sub>2</sub>O adsorbed onto it. Determining the SSA and the adsorption capacity of the soil is important to better understand the gaseous exchange between the regolith and the atmosphere, and it is also useful to constrain the nature of the hydrated amorphous phases measured by CheMin. As an illustration, in allophane, characteristic of andisols, H<sub>2</sub>O molecules are bound strongly to hydroxyl functional groups such as Si-OH and Al-OH-Al, if those are accessible to H<sub>2</sub>O molecules (66). Hydroxyl functional groups thus increase the ability of this material to adsorb water even at low relative humidities (RHs). Typically, allophane at RH = 30% can adsorb twice as much H<sub>2</sub>O as its structural hydroxyl content (70). This is also the case for the popular allophane-rich martian analog JSC Mars-1 (74).

For a given SSA, the amount of water vapor adsorbed depends on the RH, as expressed by adsorption isotherms. On sol 74/75, the dates of the day/night experiment described above, the RH observations by the REMS-H device (Rover Environment Monitoring Station–Humidity Sensor) (75) in the early morning before sunrise gave

a preliminary value of ~20% at an altitude of 1.5 m above the surface. This corresponds to an RH value of 25 to 35% at the ground level because early-morning ground temperature is 1 to 3 K lower (76) than the atmospheric temperature at the MSL boom level. Noontime RH at sol 74 was approximately 0 to 0.05% because of the noontime high atmospheric temperature.

Estimates of the SSA can be obtained using adsorption isotherms obtained on martian analogs. Adsorption isotherms were measured for several geological samples under martian conditions ( $T = 243$  K,  $RH = 0$  to 70%), together with kinetic parameters (67, 69). Figure 7 shows that to first order, the amount of H<sub>2</sub>O adsorbed is approximately linearly related to the SSA. The relative insensitivity to mineralogy for geological materials was also shown by (77). To hold <1 wt % of adsorbed H<sub>2</sub>O at  $RH = 0.001$ , the SSA should be <13 m<sup>2</sup> g<sup>-1</sup>. Similarly, to hold <1 wt % of adsorbed H<sub>2</sub>O at  $RH = 0.3$ , the SSA should be <24 m<sup>2</sup> g<sup>-1</sup>. Between  $RH = 0.001$  and  $RH = 0.3$ , the differential amount of adsorbed water is ~0.033 wt %/(m<sup>2</sup> g<sup>-1</sup>), corresponding to the different slopes in Fig. 7. Because ChemCam did not observe diurnal variations greater than ~1.1 wt %, the SSA should be lower than ~30 m<sup>2</sup> g<sup>-1</sup>. Extrapolation of the adsorption isotherms from 243 K to temperatures measured at Gale crater at night is not believed to significantly affect this upper limit, either making it a safe upper limit or possibly increasing it to ~45 m<sup>2</sup> g<sup>-1</sup>, depending on the isosteric heat of adsorption considered (34). Using the desorption branch of the isotherms published by (67) gave very similar results.

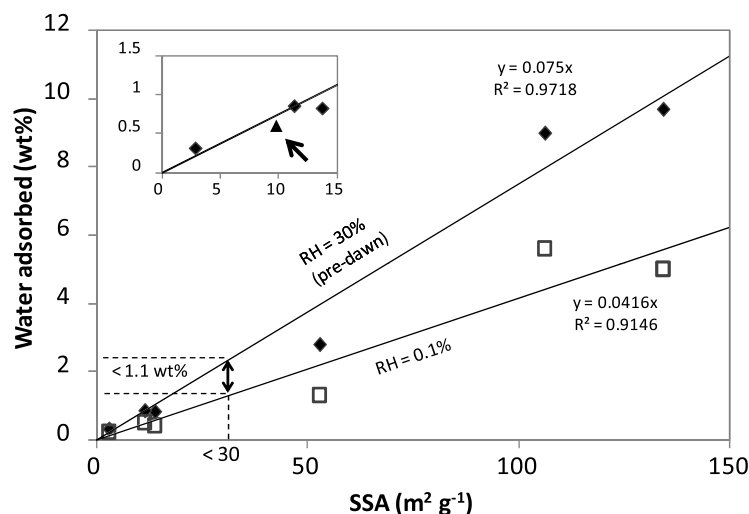


**Fig. 7. Amount of adsorbed water as a function of SSA and relative humidity.** The two curves represent linear fits through the experimental data (adsorption isotherms) measured by (67) on six geological samples at 243 K, for two values of RH (0.1% and 30%) corresponding to the conditions prevailing approximately at Gale during the day/night Crestaaurum experiment. Note that although there is some dispersion around the fits, the gaps between the experimental values and the fits (which matter here) are very similar. The double-sided arrow represents the upper limit of the difference of H<sub>2</sub>O abundance estimated by ChemCam between the two local times, which translates into an upper limit for the SSA. By increasing order of SSA, the samples are as follows: dunite (2.83 m<sup>2</sup> g<sup>-1</sup>), volcanic tuff + Mg sulfates (11.3 m<sup>2</sup> g<sup>-1</sup>), volcanic tuff (13.7 m<sup>2</sup> g<sup>-1</sup>), smectite SWy-2 (52.7 m<sup>2</sup> g<sup>-1</sup>), JSC Mars-1 (106 m<sup>2</sup> g<sup>-1</sup>), and ferrihydrite (134 m<sup>2</sup> g<sup>-1</sup>). The experimental data of (78) (arrow in the inset) obtained at 253 K with ground Vacaville basalt (2.83 m<sup>2</sup> g<sup>-1</sup>) fall well on the fit (no data available at low RH). See supplementary material for more details.

#### Spatial and Temporal Variability of the Hydrogen Signal

In order to investigate the variability of the H signal at different time and depth scales, three types of ChemCam experiments were conducted. First, we checked whether there was any gradient with depth within the first 30 shots, corresponding roughly to the first few millimeters of the subsurface. For that, a sample of 62 individual LIBS points has been analyzed. The choice of these specific points was dictated by the need to compare relatively similar, fine-grained soils. All were selected from cluster 1. The profile of each point was checked for the presence of any obvious “coarse” grains, and when it occurred, the corresponding shots were removed from the depth profile. Figure 6B shows the depth profile of the average signal-to-background (S/B) ratio of these 62 points. Within the uncertainty of the measurement (Fig. 6B), no trend with depth is observed.

To check whether the interior of the trench had a larger hydrogen signature than the exposed surface, given the lower maximal temperatures reached during the day, two sets of individual spectra were selected and compared: ~1000 spectra acquired on undisturbed soils and ~700 spectra acquired in the interior of the trench. Given the size of the data set, we preferred to perform an ICA analysis of the H component. However, it



was shown that all points plot on a mixing line between (high Na, low H) and (low Na, high H) (Fig. 5). Thus, to be comparable, the samples should have a similar Na component. The spectra corresponding to the fine-grained soil samples were selected in a range of low Na component values [the Mg/(Cr,Mn) component was also tested and gave exactly the same result]. The histograms showing the distribution of the H component for these two populations are presented in Fig. 6D. A Kolmogorov-Smirnov statistical test showed that there was no significant difference between the two populations. Therefore, we conclude that the interior of the trench does not show evidence of an H<sub>2</sub>O enrichment compared to the undisturbed surface, within the sensitivity of the measurement (34). This has an implication with regard to the relevance of the extrapolation of the SAM results to a more global scale. It means that the hydrogen content measured by SAM is comparable to the hydrogen measured over an exposed surface, typically seen by orbital measurements. We do not see evidence for a two-layer model at this scale (a few centimeters). Nonetheless, this analysis does not rule out the possibility that the interior of the trench was more hydrated when it was excavated, and it lost its additional H<sub>2</sub>O in the 11 sols between the scooping and the first measurement by ChemCam on sol 72.

Finally, we have monitored the evolution of the H signal of a freshly exposed soil (the trench in Rocknest ripple) over a 25-sol time span, 11 sols after it was scooped. The intent was to detect a possible desiccation of the exposed material. The average hydrogen S/B ratio of each LIBS point obtained for a series of four targets is plotted in Fig. 6C as a function of time, the *x* axis representing the sol at which the targets were measured: Schmutz (9 LIBS points, on sol 72), Kenyon (10 LIBS points, on sol 81), Epworth3 (12 first LIBS points, on sol 84), and Kenyon\_high\_albedo (10 LIBS points, on sol 97). Again, for each point, spectra attributed to “coarse” grains were removed. No statistically significant variation of the H signal was observed with time.

#### References and Notes

- M. H. Carr, *The Surface of Mars* (Cambridge Univ. Press, Cambridge, 2007).
- H. V. McSween Jr., I. O. McGlynn, A. D. Rogers, Determining the modal mineralogy of Martian soils. *J. Geophys. Res.* **115**, E00F12 (2010). doi: [10.1029/2010JE003582](https://doi.org/10.1029/2010JE003582)
- I. O. McGlynn, C. M. Fedo, H. Y. McSween Jr., Soil mineralogy at the Mars Exploration Rover landing sites: An assessment of the competing roles of physical sorting and chemical weathering. *J. Geophys. Res.* **117**, E01006 (2012). doi: [10.1029/2011JE003861](https://doi.org/10.1029/2011JE003861)
- W. V. Boynton *et al.*, Concentration of H, Si, Cl, K, Fe, and Th in the low- and mid-latitude regions of Mars. *J. Geophys. Res.* **112**, E12599 (2007). doi: [10.1029/2007JE002887](https://doi.org/10.1029/2007JE002887)
- S. Maurice *et al.*, Mars Odyssey neutron data: 1. Data processing and models of water-equivalent-hydrogen distribution. *J. Geophys. Res.* **116**, E11008 (2011). doi: [10.1029/2011JE003810](https://doi.org/10.1029/2011JE003810)
- R. E. Milliken *et al.*, Hydration state of the Martian surface as seen by Mars Express OMEGA: 2. H<sub>2</sub>O content of the surface. *J. Geophys. Res.* **112**, E08S07 (2007). doi: [10.1029/2006JE002853](https://doi.org/10.1029/2006JE002853)
- O. Aharonson, N. Schorghofer, Subsurface ice on Mars with rough topography. *J. Geophys. Res.* **111**, E11007 (2006). doi: [10.1029/2005JE002636](https://doi.org/10.1029/2005JE002636)
- T. Tokano, D. Bish, Hydration state and abundance of zeolites on Mars and the water cycle. *J. Geophys. Res.* **110**, 2156–2202 (2005). doi: [10.1029/2005JE002410](https://doi.org/10.1029/2005JE002410)
- C. I. Fialips *et al.*, Hydration state of zeolites, clays, and hydrated salts under present-day Martian surface conditions: Can hydrous minerals account for Mars Odyssey observations of near-equatorial water-equivalent hydrogen? *Icarus* **178**, 74–83 (2005). doi: [10.1016/j.icarus.2005.04.020](https://doi.org/10.1016/j.icarus.2005.04.020)
- F. Poulet *et al.*, Phyllosilicates on Mars and implications for early martian climate. *Nature* **438**, 623–627 (2005). doi: [10.1038/nature04274](https://doi.org/10.1038/nature04274); pmid: [16319882](https://pubmed.ncbi.nlm.nih.gov/16319882/)
- J. F. Mustard *et al.*, Hydrated silicate minerals on Mars observed by the Mars Reconnaissance Orbiter CRISM instrument. *Nature* **454**, 305–309 (2008). doi: [10.1038/nature07097](https://doi.org/10.1038/nature07097); pmid: [18633411](https://pubmed.ncbi.nlm.nih.gov/18633411/)
- J. Carter, F. Poulet, J.-P. Bibring, N. Mangold, S. Murchie, Hydrous minerals on Mars as seen by the CRISM and OMEGA imaging spectrometers: Updated global view. *J. Geophys. Res.* **118**, 831–858 (2013). doi: [10.1029/2012JE004145](https://doi.org/10.1029/2012JE004145)
- J. Carter, F. Poulet, J. P. Bibring, S. Murchie, Detection of hydrated silicates in crustal outcrops in the northern plains of Mars. *Science* **328**, 1682–1686 (2010). doi: [10.1126/science.1189013](https://doi.org/10.1126/science.1189013); pmid: [20576889](https://pubmed.ncbi.nlm.nih.gov/20576889/)
- B. L. Ehlmann *et al.*, Subsurface water and clay mineral formation during the early history of Mars. *Nature* **479**, 53–60 (2011). doi: [10.1038/nature10582](https://doi.org/10.1038/nature10582); pmid: [22051674](https://pubmed.ncbi.nlm.nih.gov/22051674/)
- D. Jouglé *et al.*, Hydration state of the Martian surface as seen by Mars Express OMEGA: 1. Analysis of the 3 μm hydration feature. *J. Geophys. Res.* **112**, E08S06 (2007). doi: [10.1029/2006JE002846](https://doi.org/10.1029/2006JE002846)
- B. C. Clark *et al.*, The Viking X ray fluorescence experiment: Analytical methods and early results. *J. Geophys. Res.* **82**, 4577–4594 (1977). doi: [10.1029/J5082i028p04577](https://doi.org/10.1029/J5082i028p04577)
- B. C. Clark *et al.*, Chemical composition of martian fines. *J. Geophys. Res.* **87**, 10059–10067 (1982). doi: [10.1029/JB087iB12p10059](https://doi.org/10.1029/JB087iB12p10059)
- H. Wänke, J. Brückner, G. Dreibus, R. Rieder, I. Ryabchikov, Chemical composition of rocks and soils at the Pathfinder site. *Space Sci. Rev.* **96**, 317–330 (2001). doi: [10.1023/A:1011961725645](https://doi.org/10.1023/A:1011961725645)
- R. Rieder *et al.*, Chemistry of rocks and soils at Meridiani Planum from the Alpha Particle X-ray Spectrometer. *Science* **306**, 1746–1749 (2004). doi: [10.1126/science.1104358](https://doi.org/10.1126/science.1104358); pmid: [15576611](https://pubmed.ncbi.nlm.nih.gov/15576611/)
- R. Gellert *et al.*, Chemistry of rocks and soils in Gusev Crater from the alpha particle x-ray spectrometer. *Science* **305**, 829–832 (2004). doi: [10.1126/science.1099913](https://doi.org/10.1126/science.1099913); pmid: [15297665](https://pubmed.ncbi.nlm.nih.gov/15297665/)
- A. S. Yen *et al.*, An integrated view of the chemistry and mineralogy of martian soils. *Nature* **436**, 49–54 (2005). doi: [10.1038/nature03637](https://doi.org/10.1038/nature03637); pmid: [16001059](https://pubmed.ncbi.nlm.nih.gov/16001059/)
- O. Gasnault *et al.*, Quantitative geochemical mapping of Martian elemental provinces. *Icarus* **207**, 226–247 (2010). doi: [10.1016/j.icarus.2009.11.010](https://doi.org/10.1016/j.icarus.2009.11.010)
- H. V. McSween Jr., What we have learned about Mars from SNC meteorites. *Meteoritics* **29**, 757–779 (1994). doi: [10.1111/j.1945-5100.1994.tb01092.x](https://doi.org/10.1111/j.1945-5100.1994.tb01092.x)
- P. R. Christensen, J. L. Bandfield, M. D. Smith, V. E. Hamilton, R. N. Clark, Identification of a basaltic component on the Martian surface from Thermal Emission Spectrometer data. *J. Geophys. Res.* **105**, 9609–9621 (2000). doi: [10.1029/1999JE001127](https://doi.org/10.1029/1999JE001127)
- A. D. Rogers, O. Aharonson, Mineralogical composition of sands in Meridiani Planum determined from Mars Exploration Rover data and comparison to orbital measurements. *J. Geophys. Res.* **113**, E06S14 (2008). doi: [10.1029/2007JE002995](https://doi.org/10.1029/2007JE002995)
- F. Poulet *et al.*, Abundance of minerals in the phyllosilicate-rich units on Mars. *Astron. Astrophys.* **487**, L41–L44 (2008). doi: [10.1051/0004-6361/200810150](https://doi.org/10.1051/0004-6361/200810150)
- K. Biemann *et al.*, Search for organic and volatile inorganic compounds in two surface samples from the chryse planitia region of Mars. *Science* **194**, 72–76 (1976). doi: [10.1126/science.194.4260.72](https://doi.org/10.1126/science.194.4260.72); pmid: [17793082](https://pubmed.ncbi.nlm.nih.gov/17793082/)
- P. H. Smith *et al.*, H<sub>2</sub>O at the Phoenix landing site. *Science* **325**, 58–61 (2009). pmid: [19574383](https://pubmed.ncbi.nlm.nih.gov/19574383/)
- S. Maurice *et al.*, The ChemCam Instrument Suite on the Mars Science Laboratory (MSL) Rover: Science objectives and mast unit description. *Space Sci. Rev.* **170**, 95–166 (2012). doi: [10.1007/s11214-012-9912-2](https://doi.org/10.1007/s11214-012-9912-2)
- R. Wiens *et al.*, The ChemCam instrument suite on the Mars Science Laboratory (MSL) rover: Body unit and combined system tests. *Space Sci. Rev.* **170**, 167–227 (2012). doi: [10.1007/s11214-012-9902-4](https://doi.org/10.1007/s11214-012-9902-4)
- Hereafter, a “shot” corresponds to a single spectrum, and a “LIBS point” is a series of spectra acquired at the same laser ablation crater (i.e., sampling location).
- No implication of the presence or absence of organic materials or living matter is intended, nor is the genesis of the deposit.
- O. Forni *et al.*, Independent component analysis classification of laser induced breakdown spectroscopy spectra. *Spectrochim. Acta B* **86**, 31–41 (2013). doi: [10.1016/j.sab.2013.05.003](https://doi.org/10.1016/j.sab.2013.05.003)
- See supplementary materials on Science Online.
- S. Clegg, E. Sklute, M. D. Dyar, J. E. Barefield, R. C. Wiens, Multivariate analysis of remote laser-induced breakdown spectroscopy spectra using partial least squares, principal component analysis, and related techniques. *Spectrochim. Acta B* **64**, 79–88 (2009). doi: [10.1016/j.sab.2008.10.045](https://doi.org/10.1016/j.sab.2008.10.045)
- R. C. Wiens *et al.*, Pre-flight calibration and initial data processing for the ChemCam laser-induced breakdown spectroscopy instrument on the Mars Science Laboratory rover. *Spectrochim. Acta B* **82**, 1–27 (2013). doi: [10.1016/j.sab.2013.02.003](https://doi.org/10.1016/j.sab.2013.02.003)
- The composition of the dust was derived from the average of all the first spectra acquired on rock targets, which are very often different from the spectra of the underlying material and are found to be very homogeneous. They also share with soils a strong H signature. A small contamination of the underlying material in the first ablation cannot be totally ruled out.
- R.C. Wiens *et al.*, Compositions determined by ChemCam along Curiosity’s traverse from Bradbury station to Glenelg in Gale crater, Mars. *Lunar Planet. Sci. Conf.* **44**, abstract 1363 (2013).
- R. M. E. Williams *et al.*, Martian fluvial conglomerates at Gale crater. *Science* **340**, 1068–1072 (2013). doi: [10.1126/science.1237317](https://doi.org/10.1126/science.1237317); pmid: [23723230](https://pubmed.ncbi.nlm.nih.gov/23723230/)
- V. Sautter *et al.*, Igneous composition variations determined by ChemCam along Curiosity’s traverse from Bradbury to Rocknest area at Gale crater, Mars. *Geophys. Res. Abstr.* **15**, EGU2013–12753 (2013).
- S. R. Taylor, S. M. McLennan, *Planetary Crusts: Their Composition, Origin, and Evolution* (Cambridge Univ. Press, Cambridge, 2009).
- These grains will be qualified qualitatively as “coarse” in the following analysis, in contrast to samples whose spectral features are typical of material that is fine-grained at the LIBS scale (34). The beam size is ~400 μm at 2.8 m, average distance to the soil targets analyzed with ChemCam.
- The notation “//” means that the ICA component relates to the Mg abundance, not to the abundance of Cr and Mn, and indicates that the latter elements are positively correlated with Mg in Rocknest soils.
- G. Kocurek *et al.*, Rocknest sand shadow at the Curiosity field site: Morphology, origin, and stabilization. *Lunar Planet. Sci. Conf.* **44**, abstract 1375 (2013).
- D. L. Bish *et al.*, X-ray diffraction results from Mars Science Laboratory: Mineralogy of Rocknest at Gale crater. *Science* **341**, 1238932 (2013).
- D. F. Blake *et al.*, Curiosity at Gale crater, Mars: Characterization and analysis of the Rocknest sand shadow. *Science* **341**, 1239505 (2013).
- L. A. Leshin *et al.*, Volatile, isotope, and organic analysis of martian fines with the Mars Curiosity rover. *Science* **341**, 1238937 (2013).
- The RMSEP on the sum of total oxides is ~11.5 wt %.
- S. Clegg *et al.*, High calcium phase observations at Rocknest with ChemCam. *Lunar Planet. Sci. Conf.* **44**, abstract 2087 (2013).

50. M. Fisk *et al.*, Missing components in chemical profiles of a sand drift in Gale crater. *Lunar Planet. Sci. Conf. 44*, abstract 2156 (2013).
51. N. Rennó *et al.*, Possible physical and thermodynamical evidence for liquid water at the Phoenix landing site. *J. Geophys. Res.* **114**, E00E03 (2009). doi: [10.1029/2009JE003362](https://doi.org/10.1029/2009JE003362)
52. Although direct quantitative estimates of H abundance by ChemCam require laboratory experiments that have not been performed, we discuss in the supplementary material some preliminary estimates of upper limits of the observations reported here based on quantitative results by SAM. These estimates thus also rely on SAM uncertainties.
53. H. E. Newsom *et al.*, Geochemistry of Martian soil and bedrock in mantled and less mantled terrains with gamma ray data from Mars Odyssey. *J. Geophys. Res.* **112**, E3S012 (2007). doi: [10.1029/2006JE002791](https://doi.org/10.1029/2006JE002791)
54. R. V. Morris *et al.*, Mössbauer mineralogy of rock, soil, and dust at Meridiani Planum, Mars: Opportunity's journey across sulfate-rich outcrop, basaltic sand and dust, and hematite lag deposits. *J. Geophys. Res.* **111**, E12S15 (2006). doi: [10.1029/2006JE002791](https://doi.org/10.1029/2006JE002791)
55. R. V. Morris *et al.*, Mössbauer mineralogy of rock, soil, and dust at Gusev Crater, Mars: Spirit's journey through weakly altered olivine basalt on the plains and pervasively altered basalt in the Columbia Hills. *J. Geophys. Res.* **111**, E12S15 (2006). doi: [10.1029/2006JE002791](https://doi.org/10.1029/2006JE002791)
56. W. Goetz *et al.*, Indication of drier periods on Mars from the chemistry and mineralogy of atmospheric dust. *Nature* **436**, 62–65 (2005). doi: [10.1038/nature03807](https://doi.org/10.1038/nature03807); pmid: [16001062](https://pubmed.ncbi.nlm.nih.gov/16001062/)
57. W. T. Pike *et al.*, Quantification of the dry history of the Martian soil inferred from in situ microscopy. *Geophys. Res. Lett.* **38**, L24201 (2011). doi: [10.1029/2011GL049896](https://doi.org/10.1029/2011GL049896)
58. R. A. Eggleton, D. B. Tilley, Hisingerite: A ferric kaolin mineral with curved morphology. *Clays Clay Miner.* **46**, 400–413 (1998). doi: [10.1346/CCMN.1998.0460404](https://doi.org/10.1346/CCMN.1998.0460404)
59. E. B. Rampe *et al.*, Allophane detection on Mars with Thermal Emission Spectrometer data and implications for regional-scale chemical weathering processes. *Geology* **40**, 995–998 (2012). doi: [10.1130/G33215.1](https://doi.org/10.1130/G33215.1)
60. S. Le Mouélic *et al.*, An iterative least squares approach to decorrelate minerals and ices contributions in hyperspectral images: Application to Cuprite (Earth) and Mars, First Workshop on Hyperspectral Image and Signal Processing: Evolution in Remote Sensing, 2009. WHISPERS, 26–28 Aug. 2009 (2009). doi: [10.1109/WHISPERS.2009.5289003](https://doi.org/10.1109/WHISPERS.2009.5289003)
61. S. Shoji, N. Masami, R. Dahlgren, *Volcanic Ash Soils: Genesis, Properties and Utilization* (Elsevier, Amsterdam, 1993).
62. Soil Survey Staff, *Soil Taxonomy: A Basic System of Soil Classification for Making and Interpreting Soil Surveys* (Natural Resources Conservation Service, U.S. Department of Agriculture, ed. 2, 1999).
63. B. M. Jakosky, The seasonal cycle of water on Mars. *Space Sci. Rev.* **41**, 131–200 (1985). doi: [10.1007/BF00241348](https://doi.org/10.1007/BF00241348)
64. B. M. Jakosky, R. M. Haberle, The seasonal behavior of water on Mars. In *Mars*, H. H. Kieffer, B. M. Jakosky, C. Snyder, M. S. Matthews, Eds. (Univ. of Arizona Press, Tucson, 1992), pp. 969–1016.
65. F. Bartoli, A. J. Poulenard, B. E. Schouler, Influence of allophane and organic matter contents on surface properties of Andosols. *Eur. J. Soil Sci.* **58**, 450–464 (2007). doi: [10.1111/j.1365-2389.2007.00899.x](https://doi.org/10.1111/j.1365-2389.2007.00899.x)
66. H. Khan *et al.*, Adsorption of water on nano-ball allophane. *Clay Sci.* **12** (suppl. 2), 261–266 (2006).
67. A. Pommerol, B. Schmitt, P. Beck, O. Brissaud, Water sorption on Martian regolith analogs: Thermodynamics and near-infrared reflectance spectroscopy. *Icarus* **204**, 114–136 (2009). doi: [10.1016/j.icarus.2009.06.013](https://doi.org/10.1016/j.icarus.2009.06.013)
68. J. Jänchen, R. V. Morris, D. L. Bish, M. Janssen, U. Hellwig, The H<sub>2</sub>O and CO<sub>2</sub> adsorption properties of phyllosilicate-poor palagonitic dust and smectites under Martian environmental conditions. *Icarus* **200**, 463–467 (2009). doi: [10.1016/j.icarus.2008.12.006](https://doi.org/10.1016/j.icarus.2008.12.006)
69. P. Beck, A. Pommerol, B. Schmitt, O. Brissaud, Kinetics of water adsorption on minerals and the breathing of the Martian regolith. *J. Geophys. Res.* **115**, E10011 (2010). doi: [10.1029/2009JE003539](https://doi.org/10.1029/2009JE003539)
70. Y. Kitagawa, Dehydration of allophane and its structural formula. *Am. Mineral.* **59**, 1094–1098 (1974).
71. L. Maltagliati *et al.*, Annual survey of water vapor behavior from the OMEGA mapping spectrometer onboard Mars Express. *Icarus* **213**, 480–495 (2011). doi: [10.1016/j.icarus.2011.03.030](https://doi.org/10.1016/j.icarus.2011.03.030)
72. E. V. Ballou, P. C. Wood, T. Wydeven, M. E. Lehwalt, R. E. Mack, Chemical interpretation of Viking Lander 1 life detection experiment. *Nature* **271**, 644–645 (1978). doi: [10.1038/271644a0](https://doi.org/10.1038/271644a0)
73. D. M. Anderson, A. R. Tice, The analysis of water in the Martian regolith. *J. Mol. Evol.* **14**, 33–38 (1979). doi: [10.1007/BF01732365](https://doi.org/10.1007/BF01732365); pmid: [522156](https://pubmed.ncbi.nlm.nih.gov/522156/)

**Acknowledgments:** This research was carried out with funding from the Centre National d'Etudes Spatiales (CNES). Work in the United States was carried out under contract from NASA's Mars Program Office. W.G. acknowledges partial funding from Deutsche Forschungsgemeinschaft grant GO 2288/1-1. This team gratefully acknowledges JPL for developing and leading this successful mission. The data reported in this paper are archived at the Planetary Data System, accessible at <http://pds-geosciences.wustl.edu/missions/msl/index.htm>.

**Supplementary Materials**  
[www.sciencemag.org/content/341/6153/1238670/suppl/DC1](http://www.sciencemag.org/content/341/6153/1238670/suppl/DC1)  
 MSL Science Team Author List  
 Supplementary Text  
 Figs. S1 to S4  
 References (74–89)

3 April 2013; accepted 15 August 2013  
 10.1126/science.1238670